Lab on a Chip

PAPER

View Article Online
View Journal | View Issue

Check for updates

Cite this: *Lab Chip*, 2017, **17**, 3654

Differential detection photothermal spectroscopy: towards ultra-fast and sensitive label-free detection in picoliter & femtoliter droplets†

Richard M. Maceiczyk, ‡ David Hess,‡ Flora W. Y. Chiu, Stavros Stavrakis and Andrew J. deMello *

Despite the growing importance of droplet-based microfluidics in high-throughput experimentation, few current methods allow the sensitive measurement of absorbance within rapidly moving droplets. To address this significant limitation, we herein present the application of differential detection photothermal interferometry (DDPI) for single-point absorbance quantification in pL- and fL-volume droplets. To assess the efficacy of our approach, we initially measure absorbance in 100 pL droplets at frequencies in excess of 1 kHz and determine a detection limit of 1.4 μmol L^{-1} for Erythrosin B ($A = 3.8 \times 10^{-4}$). Subsequently, we apply the method to the analysis of fL-volume droplets and droplets generated at frequencies in excess of 10 kHz. Finally, we demonstrate the utility of DDPI as a detection scheme for colorimetric assays. Specifically, we extract the Michaelis–Menten constant for the reaction of β-galactosidase and chlorophenol-red-β-D-galactopyranoside and monitor the metabolomic activity of a population of HL-60 cells at the single cell level. Results establish single-point absorbance detection as a powerful, sensitive and rapid alternative to fluorescence for a wide range of assays within segmented flows.

Received 3rd September 2017,
Accepted 27th September 2017

DOI: 10.1039/c7lc00946a

rsc.li/loc

Published on 02 October 2017. Downloaded by ETH-Zurich on 12/13/2018 3:44:42 PM.

Recent years have seen the establishment of droplet-based microfluidic systems as exceptional tools for high throughput experimentation in the biological and chemical sciences,[1–7] providing for significant improvements in analytical throughput, assay efficiency (through enhanced heat and mass-transport), unit cost and operational flexibility. That said, the efficient detection, quantitation and analysis of molecular species remains a significant challenge due to the small sample volumes and reduced optical path-lengths associated with microfluidic environments.[8] To date, the vast majority of studies utilizing microfluidic tools employ laser-induced fluorescence as the detection modality of choice. The popularity of fluorescence detection owes much to its facile integration with microfluidic-based formats, its exquisite sensitivity (down to the single-molecule level), high information content and ability to operate on ultra-short timescales (thus allowing access to rapidly occurring processes).[9–14] That said, photobleaching, quenching and saturation effects often pose significant challenges to the extraction of quantitative information when performing time-integrated measurements.[15–17] Moreover, the efficient use of fluorescence-based detection at low analyte concentrations requires the presence of molecules with high fluorescence quantum efficiencies. Although the number of synthetic fluorophores available to the experimentalist is vast, and almost any biological, chemical or physical process can be monitored through the addition of a fluorescent moiety, this always presents an intrusion to the system under study. In this respect, it is clearly desirable to develop alternative detection strategies that provide for the rapid and sensitive detection of analyte molecules in a label-free manner.[18,19]

UV-visible absorption spectroscopy is widely used in chemical analysis for the quantitative determination of molecular species, either through the measurement of light attenuation at the resonant wavelength of a chromophore or indirectly through colorimetric assays. Its operational and instrumental simplicity has made it extremely popular for a diversity of macro- and microscale applications (since the majority of small molecules exhibit appreciable absorption in the UV and visible regions of the electromagnetic spectrum).[20] Moreover, when compared to fluorescence-based techniques, absorbance spectroscopy is less susceptible to bleaching and saturation, due to the higher photostability of non-fluorescent analytes and the associated rapid relaxation kinetics.[21] However, the performance and application of absorbance spectroscopy within microfluidic systems is compromised by reduced optical pathlengths, which directly

Institute for Chemical and Bioengineering, Department of Chemistry and Applied Biosciences, ETH Zürich, Vladimir-Prelog-Weg 1, 8093 Zürich, Switzerland. E-mail: andrew.demello@chem.ethz.ch

† Electronic supplementary information (ESI) available. See DOI: 10.1039/c7lc00946a

‡ R. M. M. and D. H. contributed equally to this work.

This journal is © The Royal Society of Chemistry 2017

Published on 02 October 2017. Downloaded by ETH-Zurich on 12/13/2018 3:44:42 PM.

impact both sensitivity and concentration detection limits.[22] This issue is especially problematic when probing pL-volume droplets moving at high linear velocities through microfluidic channels, and has severely limited the application of absorbance spectroscopy in microfluidic environments. To date, two main approaches have been used to overcome pathlength issues in droplet-based microfluidic systems. The first relies on modifying the fluidic path to stretch the droplet and increase the optical pathlength by using Z- or U-shaped channel structures.[23–26] Such approaches typically access concentration detection limits in the high micromolar range. In contrast, multi-pass and cavity enhanced techniques increase the effective optical pathlength by directing the optical beam multiple times through the analyte solution, yielding detection limits in the nanomolar range,[27–30] but at the expense of infrastructural and fluidic complexity. Additionally, it should not be forgotten that performance may be enhanced by incorporating on-chip optical components, such as micro-lenses and apertures, which act to both reduce stray light and increase the effective optical pathlength.[31] Significantly however, to date there has not been any report of a method that is able to quantify absorbance in droplets at the kilohertz frequencies typically used in microfluidic experiments.

Herein, we present the use of Differential Detection Photothermal Interferometry (DDPI), a technique recently introduced in our laboratories, as a method for high-throughput, high-sensitivity absorbance detection in microdroplets.[32] As we will describe, DDPI allows for quantitative, single-point absorbance detection in fL-pL volume droplets at speeds and with detection limits comparable to fluorescence. Photothermal spectroscopies, involving the optical detection of heat released by non-radiative relaxation of an excited-state species, are particularly well suited for application in microfluidic and nanofluidic environments due to their exceptional sensitivity in detecting absorbing species such as single nanoparticles and molecules.[33,34] Unlike techniques based on light attenuation, signals in photothermal spectroscopies are only weakly dependent on the optical pathlength, making them highly suitable for integration with microfluidic channels. Surprisingly, there have not been any reports describing the application of photothermal spectroscopies to the high-throughput analysis of droplets. We attribute this state of affairs to a number of challenges associated with such measurements.

First, at the droplet generation frequencies typical of microfluidic systems droplets will reside in the excitation volume for less than a millisecond. Accordingly, the measurement bandwidth must be large enough to capture the passing droplet and the excitation laser frequency high enough for the fluid to be quasi-stationary with respect to the oscillation of the thermal lens. Second, transiting droplets may introduce significant noise (at frequencies up to several tens of kilohertz) depending on the droplet generation frequency. Finally, even when using refractive index matched continuous and discrete phases, a passing droplet will introduce a significant phase shift of the probe beam, which will interfere with noise cancellation in interferometric methods.[35] Herein, we describe the use of DDPI in droplet-based absorbance measurements and discuss how the aforementioned challenges can be nullified in a simple and direct fashion. Moreover, we explore accessible detection limits (in both pL- and fl-volume droplets) and apply the method to two high-throughput colorimetric assays.

Results and discussion

As previously described, DDPI allows the quantitative extraction of absorbance based on a phase shift caused by the photothermal effect.[32] Briefly, a probe beam of a wavelength not absorbed by the analyte (632 nm in the current case) is split into a probe and a reference arm. An intensity modulated excitation beam of a wavelength resonant with an absorption band of the analyte (532 or 460 nm in the current case) propagates collinearly with the probe arm. A microscope objective focuses the probe arm into the centre of a microfluidic channel carrying droplets and the reference arm at the side of the channel (Fig. 1a). After transit through the microfluidic device, the probe and reference beams are collected and superimposed. Subsequently, a polarizing beam splitter projects the vertical and horizontal polarization components onto two amplified photodiodes connected to the differential input of a lock-in amplifier. The lock-in amplifier demodulates the voltage induced by the incoming light to provide the photothermal signal. This signal is linearly dependent on the optical path difference between the probe and reference arms (introduced by the photothermal effect) and therefore on the analyte concentration. The polarization states of probe and reference arm as well as the final superposition are chosen to provide exclusive sensitivity to the phase of the photothermal signal. Fig. 1b contains a schematic of the entire setup, indicating the polarization state of radiation as it propagates through the interferometer.

Droplets passing the reference arm induce an additional phase shift, which is much larger than the photothermal signal itself. We observe this phase shift and thus the time during which the droplets reside in the excitation laser (independent of analyte concentration) in the DC signal entering the lock-in amplifier prior to demodulation. To ensure linearity of the signal and efficient noise cancellation, the second Wollaston prism is aligned to provide a phase shift of π when a droplet is in the probe beam path (*i.e.* the phase sensitive alignment is corrected for the phase shift induced by the droplets). We can use the DC signal for low concentrations, where the direct identification of droplets from the photothermal signal is not possible. In such a case, we identify the beginning and end of each droplet from the DC signal, with the photothermal signal extracted from the corresponding period in the demodulated photothermal trace (Fig. S1†). The periodic phase shift caused by droplets also introduces significant noise originating at the droplet generation frequency, with harmonics spanning several tens of kilohertz. Accordingly, it is important to choose an excitation modulation

Published on 02 October 2017. Downloaded by ETH-Zurich on 12/13/2018 3:44:42 PM.

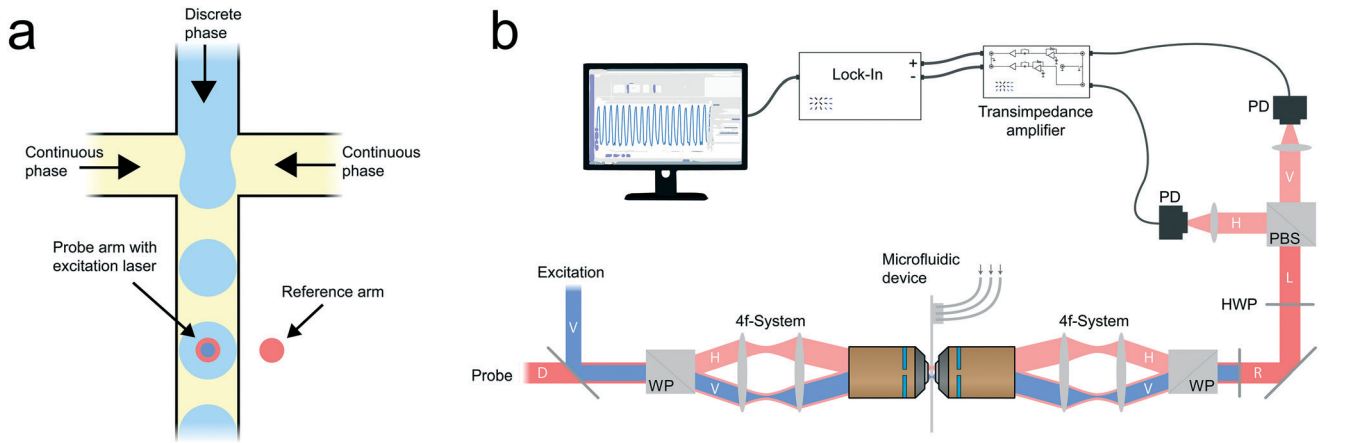

Fig. 1 DDPI for high-throughput absorbance measurements in droplets. (a) Beam spot alignment for droplet absorbance measurements with respect to a microfluidic channel. (b) Schematic drawing of the setup used in this work. WP: Wollaston prism, HWP: half-wave plate, PBS: polarizing beam splitter, PD: photodiode. The white letters in the beams indicate their polarization state. D: diagonal, V: vertical, H: horizontal, R: right-circular, L: left-circular polarized.

frequency high enough to prevent "leakage" of droplet-induced oscillations into the measurement bandwidth.

Method validation

To confirm the linear dependence of the photothermal signal on analyte concentration, evaluate concentration detection limits and estimate the measurement error, we analyzed 100 pL-volume droplets containing Erythrosin B diluted in Tris buffer (2 mmol L^{-1}, pH 9.0, ε_{532} = 78 000 ± 1200 L cm^{-1} mol^{-1}). Analyte concentrations were varied between 0 and 88 μmol L^{-1} at frequencies up to 1 kHz within in a 35 × 50 μm cross-section microfluidic channel (device designs and experimental details are provided in section S2†). At a frequency of

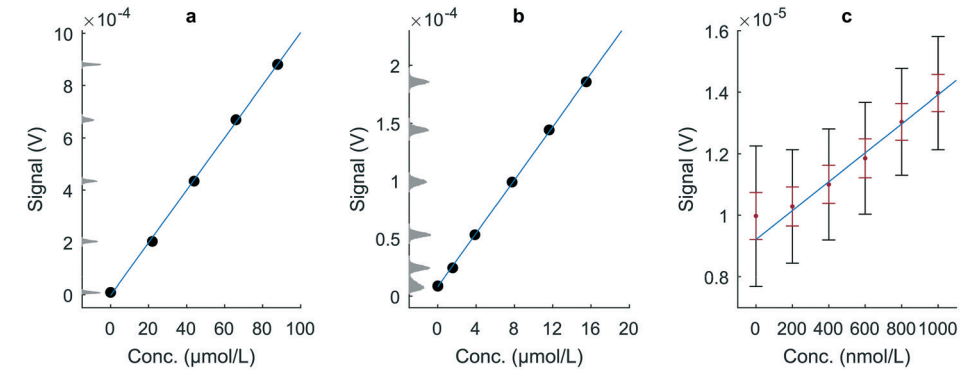

d

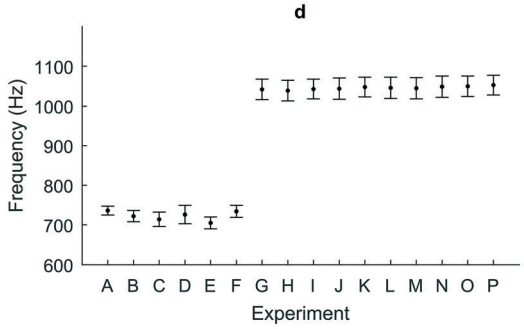

e

Experiment	Conc. (μmol/L)	Signal (μV)	Frequency (Hz)
A	0.0	10.0 ± 2.3	736 ± 11
B	0.2	10.3 ± 1.8	722 ± 14
C	0.4	11.0 ± 1.8	714 ± 18
D	0.6	11.9 ± 1.8	726 ± 23
E	0.8	13.0 ± 1.7	705 ± 15
F	1.0	14.0 ± 1.8	734 ± 15
G	0.0	8.7 ± 2.9	1042 ± 26
H	1.6	24.3 ± 2.1	1039 ± 26
I	3.9	53.1 ± 2.0	1043 ± 25
J	7.8	98.9 ± 2.4	1044 ± 27
K	11.6	144.1 ± 2.1	1048 ± 25
L	15.5	185.6 ± 2.2	1046 ± 27
M	22.0	203.1 ± 3.6	1045 ± 27
N	44.0	434.3 ± 3.7	1049 ± 27
O	65.9	669.7 ± 4.4	1050 ± 26
P	87.9	880.7 ± 2.8	1053 ± 25

Fig. 2 Calibration experiments to determine detection limits of DDPI. (a) and (b) Dependence of the average photothermal signal on Erythrosin B concentration from 0 to 88 μmol L^{-1} at a droplet frequency of 1 kHz. The standard errors are smaller than the markers. Histograms of all signals are plotted on the *y*-axes. (c) Determination of the detection limit of DDPI for droplet absorbance at a droplet frequency of 700 Hz. Black error bars correspond to the standard deviation of individual droplet signals and red error bars to the standard deviation when averaging over 10 droplets at a time. The adjusted *r*-square of each linear fit in (a)–(c) is larger than 0.99. Standard deviations were determined from the signals of at least 10 000 droplets. The linear fit in (c) excludes the point at 0 μmol L^{-1}. (d) Frequencies for each experiment as detailed in the table in (e).

 This journal is © The Royal Society of Chemistry 2017

Published on 02 October 2017. Downloaded by ETH-Zurich on 12/13/2018 3:44:42 PM.

1 kHz the droplets spend approximately 400 μs within the detection probe volume. The concentration of the droplets is adjusted directly on-chip by mixing streams of stock erythosin B solution and buffer at the desired ratios. A 532 nm laser modulated at 100 kHz is used as the excitation source. To reduce scattering artefacts and facilitate analysis of the DC time trace, a refractive index matched continuous phase (containing two parts FC-40 with 1% Raindance surfactant and one part 1,3-bis(trifluoromethyl)-5-bromobenzene) is used in all experiments.[36] For each concentration, signals are collected from at least 10 000 droplets to determine the mean signal and standard deviation. Fig. 2 reports the results of such calibration measurements. The mean photothermal signal varies linearly with concentration over the entire concentration range investigated (Fig. 2a and b) with standard deviations between 2 and 4.4 μV; close to the estimated shot noise of approximately 1 μV. We attribute any excess variance in the photothermal signal, especially at higher concentrations, to the limited dosing precision of syringe pumps.

Subsequently, droplets containing analyte at concentrations between 0 to 1 μmol L^{-1} and at a generation frequency of approximately 720 Hz (corresponding to a 900 μs droplet residence time in the probe volume) were used to determine the concentration detection limit of the system (Fig. 2c). In this experiment, relative concentration variations are negligible and a measurement error of 1.8 μV is consistently observed. The background signal for empty droplets is 10.0 ± 2.2 μV. Significantly, this leads to a detection limit of 1.4 μmol L^{-1} Erythrosin B (16 μV) with an attenuation coefficient of 0.11 cm^{-1} for individual droplets. Considering that the optical pathlength (through a droplet) is at most 35 μm, the minimum detectable absorbance (A) is 3.8×10^{-4}. Such a detection limit is approximately one order of magnitude higher than the best (chip-based) fluorescence detector at comparable droplet frequencies, if normalized to the droplet diameter.[10] A more sophisticated setup incorporating orthogonal line confocal excitation and single-photon avalanche photodiode detection has reported a concentration detection limit of 250 pM in 30 μm droplets, but at significantly lower droplet frequencies (60 Hz). Indeed, droplet generation frequencies essentially define the limits for fluorescence detection in droplets without resorting to significant alterations of channel structure.[11] To further decrease detection limits in our system it is possible either to slow down droplets (thus decreasing the necessary measurement bandwidth) or to average signals over multiple droplets. We illustrate this by averaging the signal over ten droplets at a time (shown by the red error bars in Fig. 2c). This approach leads to a detection limit of 570 nmol L^{-1} (12 μV), and despite the loss of single droplet information, is valuable in applications where analyte concentrations in the droplets are constant over multiple droplets.

To demonstrate quantitative individual droplet detection, six equally large populations of droplets containing 0, 20, 40, 60, 80 and 100 μmol L^{-1} Erythrosin B were generated and then combined in a random fashion off-chip. Subsequently, the mixed population was reinjected into a 30 × 50 μm cross-section microfluidic channel integrated with DDPI. The resulting histogram of droplet signals provided in Fig. 3 unmistakeably identifies the six underlying component populations. We believe that some exchange of analyte between the droplets during storage causes a slight broadening of the signal distributions within the different populations. Importantly, the occupancy of the individual populations is in excellent agreement with the theoretical value of 16.7%. This result confirms that our method is highly valuable in applications requiring long-term incubation off-chip prior to detection (for example, in directed evolution experiments) or within combinatorial assays.[37,38]

Analysis of small droplets and droplets moving at high linear flow velocities

The quantitative analysis of fL volume droplets is of significant importance in a range of large-scale experimental applications, such as digital microfluidics and single enzyme (or bacteria) screening, since analyte concentrations scale inversely with droplet volume. In these applications, the ability to assay large numbers of droplets is essential in obtaining statistically significant data, with the low detection limit of DDPI being necessary for binary classification and sorting.[39,40] Since DDPI signals do not depend on the optical pathlength to any appreciable extent, with the largest part of the phase shift being generated in the focal point of the probe laser, droplet size will only weakly influence the photothermal signal as long as droplets remain larger than the focal volume (approximately 1 fL). In fact, small droplets are in some respects favourable, since the optical path difference between probe and reference beam introduced by the droplets decreases with droplet size, therefore causing less interference. To demonstrate such behaviour, we produced droplets containing 40 μmol L^{-1} Erythrosin B and motivated them through a 5 × 4 μm cross-section channel. Individual droplets in this case are approximately 120 fL in volume, generated at a frequency of 996 ± 9 Hz and have a residence time of 250 ± 4 μs in the detection probe volume. To match the refractive index of droplets and the continuous phase (silicone oil, 10 cSt), 53% (w/w) glycerol and 47% (w/w) 2 mmol L^{-1} Tris buffer comprise the analyte solution. Refractive index matching *via* addition of a high refractive index liquid to the continuous phase is not possible since the refractive index of silicone oil is higher than water. The switch to a silicone oil continuous phase (which has a higher viscosity than FC-40) facilitates the production of monodisperse fL-volume droplets at frequencies below 10 kHz and at high water-to-oil ratios. Fig. 4a presents a section of the time trace of the photothermal signal and Fig. 4b illustrates a histogram of the collected photothermal signals. It can be seen that appreciable noise is observed between droplets (due to the large bandwidth of the measurement), but it is important to note

Published on 02 October 2017. Downloaded by ETH-Zurich on 12/13/2018 3:44:42 PM.

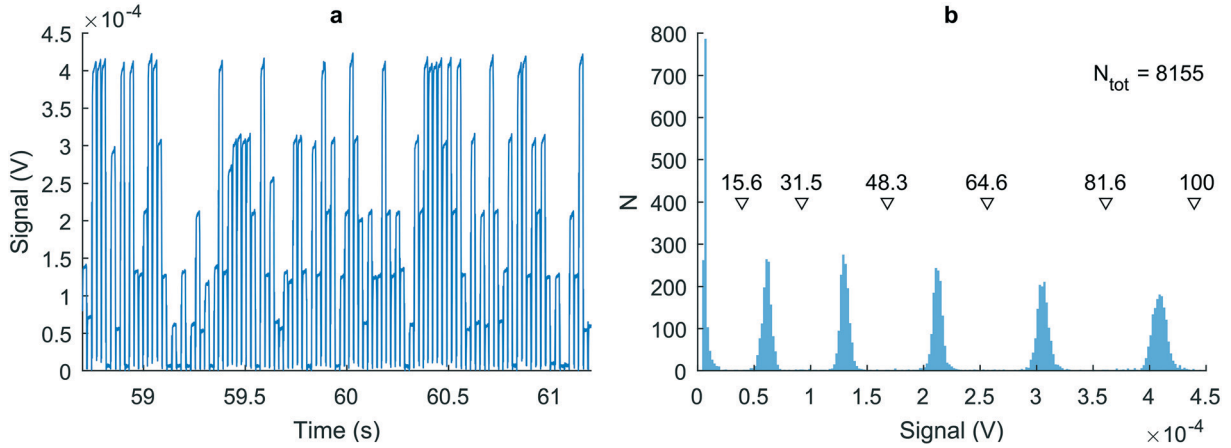

Fig. 3 Random reinjection and detection of six droplet populations with different concentrations of Erythrosin B. (a) Time-trace of the photothermal signal showing the different signal levels of the droplets. (b) Histogram of photothermal signal of the individual droplets clearly revealing the six populations. The numbers above the triangles indicate the percent of droplets below the indicated signal level.

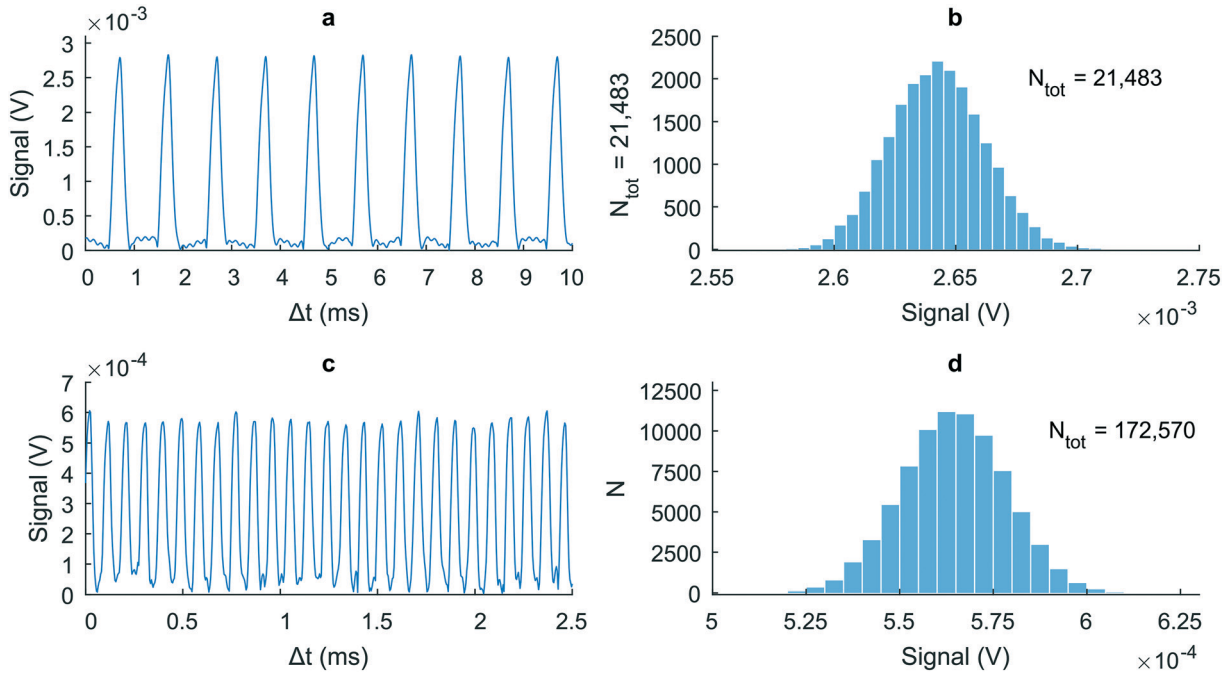

Fig. 4 Analysis of small droplets and droplets moving at high linear flow velocities. (a) Time trace of the photothermal signal and (b) histogram of individual droplet signals for 120 fL droplets containing 40 μmol L^{-1} Erythrosin B. The droplets propagate at a frequency of about 1 kHz. (c) Time trace of the photothermal signal and (d) histogram of individual droplet signals for droplets passing the excitation beam with a frequency of 10.7 kHz containing 20 μmol L^{-1} methyl orange.

that this noise does not influence the achievable detection limits. As described previously, the relative phases of the two interferometer arms are aligned to ensure maximal noise cancellation when a droplet resides within the probe beam. Accordingly, the interferometer is out of alignment with the probe beam when passing between droplets, and thus negligible noise cancellation takes place. The average signal over all 21 483 droplets is 2.64 ± 0.02 mV (A = 1.3 × 10^{-3}). The higher photothermal signal compared to the calibration experiment originates from a higher incident probe laser power on the photodiodes together with a larger temperature coefficient of the refractive index in glycerol. The relative standard deviation of 0.8% in this experiment is in excellent agreement with calibration experiments at a concentration of 44 μmol L^{-1}, where we obtained a relative error of 0.9%. This result confirms a detection limit of 1.4 μmol L^{-1} Erythrosin B in the case of fL-volume droplets.

For measurements up to a droplet frequency of 1 kHz, a laser modulation frequency of 100 kHz is sufficient, both in terms of the fluid flow effect on the thermal lens and

 This journal is © The Royal Society of Chemistry 2017

Published on 02 October 2017. Downloaded by ETH-Zurich on 12/13/2018 3:44:42 PM.

separation of the measurement bandwidth from noise caused by the droplets. To allow measurements at even higher droplet frequencies the modulation of the excitation laser was increased to 1 MHz. Since the 532 nm laser is limited to 100 kHz at full extinction ratio, it was replaced with a faster 460 nm diode laser, with a 20 μmol L^{-1} methyl orange solution in water (ε_{460} = 25 400 ± 300 L cm^{-1} mol^{-1}) being used as the analyte. Using the same device and continuous phase as in the calibration experiments, we generated 100 pL-volume droplets at a frequency of 10.7 ± 0.3 kHz, corresponding to a droplet residence time in the probe volume of 46 ± 3 μs. Using this setup the absorbance of 172 570 individual droplets (A = 2.5 × 10^{-4}) were measured in 16 seconds, yielding an average photothermal signal of 564 ± 14 μV. Fig. 4c and d illustrate an exemplar time trace and frequency histogram of all signals. The relative standard deviation of 2.5% remains exceptionally low but is higher than in previous experiments due to a larger measurement bandwidth. The signal error together with the high sensitivity and speed of our method has the potential to replace fluorescence in applications such as droplet sorting, allowing sharp distinction between two or more droplet populations.

On-chip colorimetric assays

To demonstrate the application of DDPI to more relevant and complex biological problems, we performed colorimetric assays monitoring the reaction between β-galactosidase (a blue-white screening reporter monitoring gene expression) and chlorophenol-red-β-D-galactopyranoside at room temperature.[41–43] Specifically, enzyme and substrate (diluted to different concentrations) were mixed off-chip. To allow for data collection at different time points, the microfluidic device integrates several interrogation points separated by delay lines. Initial reaction rates were extracted for each substrate concentration from a plot of signal *versus* time by fitting to the Michaelis–Menten equation, $v = v_{max}[S]/(K_M + [S])$ (Fig. 5a and b). Here, v is the reaction rate, v_{max} the maximal reaction rate, [S] the substrate concentration and K_M the Michaelis–Menten constant. From such a fit we determined a Michaelis–Menten constant of 990 μmol L^{-1}. Bulk experiments performed using a benchtop spectrometer (Fluoromax-4, Jobin Yvon Technologies) yield a value of 910 μmol L^{-1}, which is in excellent agreement with the microfluidic data (ESI† S3).

Droplet-based microfluidic systems are ideal platforms for performing high-throughput experiments at the single-cell level,[44,45] since individual cells can be encapsulated with defined amounts of reagent or substrate in a controllable manner. Such an approach combined with DDPI accordingly allows the performance of single cell colorimetric assays in applications such as directed evolution and drug, growth factor or toxin screening.[46] To this end, we used DDPI to determine the metabolic activity distribution within a population

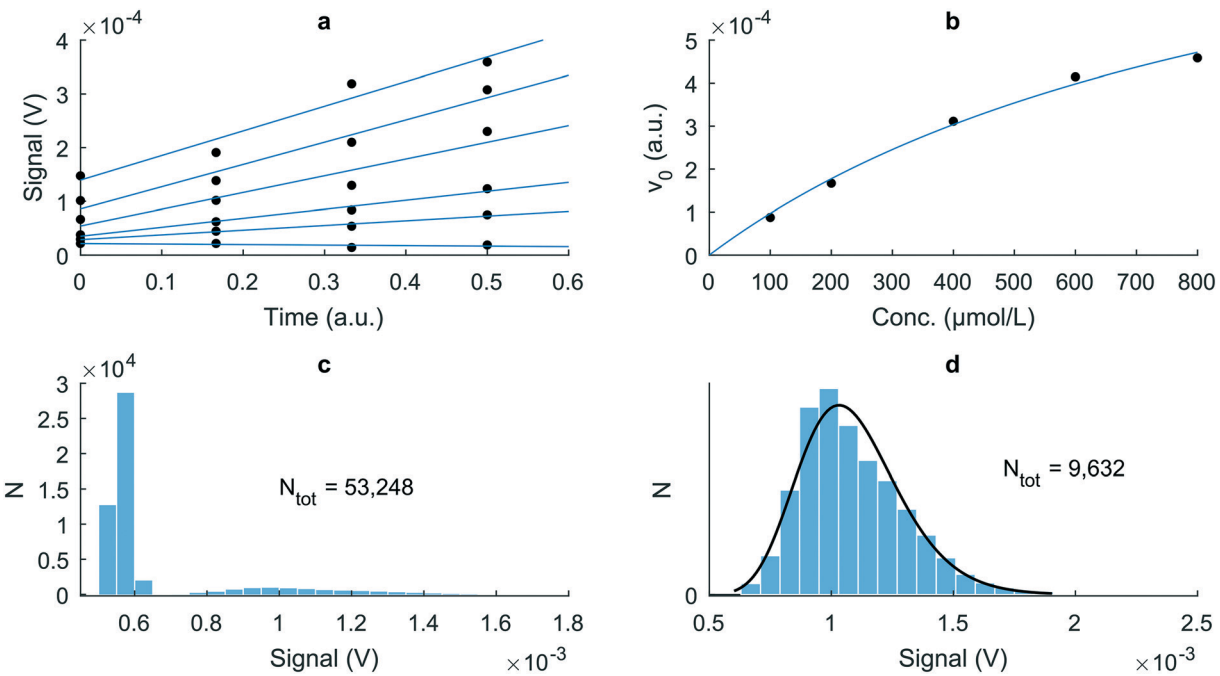

Fig. 5 Colorimetric assays performed in droplets using DDPI as detector. (a) Signal *vs.* time plot to extract initial rates of reaction for the reaction between β-D-galactosidase and chlorophenol-red-β-D-galactopyranoside. The markers are larger than one standard deviation of the individual droplet signals. The substrate concentrations corresponding to the fits are 0, 100, 200, 400, 600 and 800 μmol L^{-1}. the signals at time zero vary due to background absorbance of unreacted substrate. (b) Michaelis–Menten plot of the obtained rate constants and fit of the Michaelis–Menten equation. (c) Histogram of all droplet signals obtained in the single-cell metabolomics activity assay using the cell proliferation reagent WST-1. The droplets with a signal higher than 6.5 × 10^{-4} contain cells. (d) Histogram of the cell containing droplets. The black curve is a fit of a lognormal distribution to the data.

Published on 02 October 2017. Downloaded by ETH-Zurich on 12/13/2018 3:44:42 PM.

of HL-60 cells. Briefly, we encapsulated cells (experimentally determined viability immediately before the experiment >99%) with the cell proliferation reagent WST-1 (Roche Diagnostics) and adjusted the cell concentration to yield an occupancy (droplets containing one or more cells) of approximately 20%. Droplets were incubated on-chip using delay chambers for a period of 20 minutes, and subsequently probed at 460 nm. The use of delay chambers prevent variations in reaction time between droplets, so that any differences in the photothermal signal are exclusively due to differences in activity.[47] WST-1 reacts *via* an electron-mediator with mitochondrial succinate-tetrazolium reductase forming a Formazan dye, which reports metabolic activity of the cell through variations in absorbance.[48] Importantly, reagent does not enter the cells to a significant extent, ensuring minimal toxicity and allowing long-term incubation. Analysis of absorbance signals from 53 248 individual droplets yields the frequency histograms presented in Fig. 5c and d. These data indicate that 18.1% (9632 droplets) have an absorbance value distinct from an empty droplet. This fraction corresponds well with the experimental cell occupancy determined *via* brightfield imaging (of 0.23 cells per droplet). The signal distribution of cell-containing droplets reveals a log-normal distribution as is expected for intra-cellular reaction dynamics.[49] We attribute minor deviations from a lognormal distribution to the fact that about 10% of the droplets containing cells are doubly occupied. Importantly, since a wealth of absorbance-based assays are now commercially available for screening cells, enzymes and bacteria, such assays can be directly transferred to our microfluidic platform for operation in high-throughput.

In conclusion, we have presented DDPI as a sensitive, rapid and label-free detection method for use with droplet-based microfluidic systems. Initial calibration studies confirm the utility of DDPI in content analysis with a detection limit of 1.4 μmol L^{-1} at a frequency of 1 kHz. Concentration detection limits could be further reduced to nM levels through simple averaging over droplets. The unprecedented sensitivity of DDPI also allows single point absorbance measurements of femtoliter droplets or droplets produced at frequencies in excess of 10 kHz. Since no modifications to standard single-layer microfluidic networks are necessary, single point DDPI measurements represent a powerful and high-efficiency alternative to fluorescence-based detection in molecular analysis. Achievable measurement frequencies and detection limits mean that absorbance-based methods can for the first time be employed in applications where fluorescence detection currently dominates (such as directed evolution of enzymes, enzyme kinetics, droplet sorting and single cell analysis[38,50,51]). The colorimetric assays presented for the analysis of enzyme kinetics and single cell activity provide compelling examples of possible applications.

We envision a variety of future applications for DDPI that take advantage of its unique capabilities. The pathlength independence of DDPI allows for the detection of analytes in a "volume independent" manner, which in turn enables large-scale, digital enzymatic assays in femtoliter droplets through colorimetric monitoring at kHz frequencies. Moreover, the ability to perform precise, rapid yet miniaturized assays will prove invaluable not only in a variety of directed evolution applications, but also for exploring metagenomic and genomic library diversity. Building on the model single cell activity assay presented herein it will be possible to monitor the effects of drugs, toxins or other stresses on cell metabolism at the single cell level and in high throughput. The combination of single cell detection with low concentration drug dosing is a highly promising approach for understanding the effects of therapeutic treatments as part of early stage drug candidate screens and personalized medicine therapies that could otherwise be missed in bulk cell population analyses.

Methods

Differential detection photothermal interferometry

The beam of a 632 nm HeNe laser (21.5 mW) is spatially filtered, expanded and its polarization adjusted to diagonal. Intensity modulated light from a 532 nm solid-state laser (120 mW) is spatially filtered, expanded and its polarization adjusted to vertical. Both beams are combined at a dichroic mirror before entering a Wollaston prism, with the optic axes of its crystals oriented at ±π/4 with respect to the polarization of the red beam. The prism splits and directs the red beam into the reference and probe arm of an interferometer, with equal intensity and perpendicular polarization, and the green beam is directed collinear with the probe arm. A 4f-system constructed from a scan and a tube lens couples the light into a microscope objective (NA 0.75, 40×) resulting in two focal volumes laterally separated by approximately 40 μm. The focal volume corresponding to the probe arm lies at the centre of a microfluidic channel carrying droplets to be analysed, while the reference arm focuses besides the channel within the substrate material. The position of the microfluidic channel is adjusted by mounting the microfluidic device onto a precision *xyz*-stage. After transit, a second objective and 4f-system directs the beams into a second Wollaston prism oriented to superimpose the two arms of the interferometer producing right-circular polarized light. The light passes a half wave plate with its fast axis oriented at +π/8 and subsequently a polarizing beam splitter with its transmission axis oriented at +π/4 (both orientations with respect to the initial red beam polarization). Two photodiodes connected to a current amplifier (HF2TA, Zurich Instruments, Switzerland) and differential input of a lock-in amplifier (HF2LI, Zurich Instruments, Switzerland) receive the two polarization components exiting the polarizing beam splitter. The green beam is intensity modulated *via* the signal output of the lock-in amplifier. The demodulated signal as well as the DC component received by the lock-in are recorded and analysed off-line using an in-house MatLab® program.

 This journal is © The Royal Society of Chemistry 2017

Published on 02 October 2017. Downloaded by ETH-Zurich on 12/13/2018 3:44:42 PM.

Microfluidic device fabrication

Microfluidic channel networks are designed using AutoCAD® and used to generate film or glass photomasks. Master SU-8 moulds of desired heights are created using conventional photolithographic techniques that have been described in detail elsewhere.[52]

Subsequently, a 10 : 1 (w/w) mixture of polydimethylsiloxane (PDMS) and curing agent (Sylgard 184, Dow Corning, Midland, USA) is degassed in a desiccator for 45 minutes, and then spin-coated on the master mould at 350 rpm for 30 seconds. After allowing the PDMS layer to equilibrate (15 minutes at room temperature) the wafer is placed in an oven at 70 °C for a further 45 minutes. 7 mm thick PDMS squares are then bonded on top of the designed inlets using an oxygen plasma. To strengthen bonding, the wafer is placed on a hotplate at 120 °C for 15 minutes. Subsequently, the PDMS is carefully detached from the master mould and diced to form individual devices. Holes for inlets and outlets are punched at the desired positions, and devices cleaned using detergent and deionized water followed by sonication in methanol for 5 minutes. Devices are then dried under N_2 flow and bonded to PDMS coated glass cover slips in an oxygen plasma. After waiting one minute to obtain an adequate bonding strength, a solution of 5% (v/v) dodecyltriethoxysilane in isopropanol is injected into the formed microchannels and incubated 5 minutes at room temperature. The solution is then removed by connecting the outlet to vacuum and devices placed on a hotplate at 120 °C for 2 hours. Finally, 2 × 3 mm coverslip sections are bonded in an air plasma on top of the devices covering the detection area.

Cell culture and preparation

HL-60 cells are cultured in RPMI 1640 medium, supplemented with 10% (v/v) fetal bovine serum, 2 mM L-glutamine (Invitrogen, UK), 50 U mL^{-1} penicillin and 50 μg mL^{-1} streptomycin (Invitrogen, UK). All cell cultures are sustained in a 5% CO_2 humidified atmosphere at 37 °C.

Prior to experimentation, cells are washed once with calcium- and magnesium-free phosphate-buffered saline (CMF-PBS; Invitrogen, UK), and counted with a haemocytometer. Cells were then centrifuged and re-suspended in pre-warmed RPMI medium (without Phenol red; Invitrogen, UK), at the preferred concentration. Finally, cells are fed with 17% (v/v) OptiPrep™ density gradient medium (Sigma Aldrich, Switzerland) to avoid undesirable cell sedimentation over the timescale of experimentation.

Conflicts of interest

There are no conflicts to declare.

References

1 K. S. Elvira, X. Casadevall i Solvas, R. C. R. Wootton and A. J. deMello, The Past, Present and Potential for Microfluidic Reactor Technology in Chemical Synthesis, *Nat. Chem.*, 2013, **5**, 905–915.
2 I. Lignos, S. Stavrakis, A. Kilaj and A. J. deMello, Millisecond-Timescale Monitoring of PbS Nanoparticle Nucleation and Growth Using Droplet-Based Microfluidics, *Small*, 2015, **11**, 4009–4017.
3 I. Lignos, *et al.*, Synthesis of Cesium Lead Halide Perovskite Nanocrystals in a Droplet-Based Microfluidic Platform: Fast Parametric Space Mapping, *Nano Lett.*, 2016, **16**, 1869–1877.
4 R. M. Maceiczyk, L. Bezinge and A. J. deMello, Kinetics of Nanocrystal Synthesis in a Microfluidic Reactor: Theory and Experiment, *React. Chem. Eng.*, 2016, **1**, 261–271.
5 R. M. Maceiczyk and A. J. deMello, Fast and Reliable Metamodeling of Complex Reaction Spaces Using Universal Kriging, *J. Phys. Chem. C*, 2014, **118**, 20026–20033.
6 R. M. Maceiczyk, I. G. Lignos and A. J. deMello, Online Detection and Automation Methods in Microfluidic Nanomaterial Synthesis, *Curr. Opin. Chem. Eng.*, 2015, **8**, 29–35.
7 D. T. Chiu, *et al.*, Small but Perfectly Formed? Successes, Challenges, and Opportunities for Microfluidics in the Chemical and Biological Sciences, *Chem*, 2017, **2**, 201–223.
8 Y. Zhu and Q. Fang, Analytical Detection Techniques for Droplet Microfluidics - a Review, *Anal. Chim. Acta*, 2013, **787**, 24–35.
9 P. S. Dittrich, M. Jahnz and P. Schwille, A New Embedded Process for Compartmentalized Cell-Free Protein Expression and On-line Detection in Microfluidic Devices, *ChemBioChem*, 2005, **6**, 811–814.
10 F. Guo, *et al.*, A Droplet-Based, Optofluidic Device for High-Throughput, Quantitative Bioanalysis, *Anal. Chem.*, 2012, **84**, 10745–10749.
11 G. D. M. Jeffries, R. M. Lorenz and D. T. Chiu, Ultrasensitive and High-Throughput Fluorescence Analysis of Droplet Contents with Orthogonal Line Confocal Excitation, *Anal. Chem.*, 2010, **82**, 9948–9954.
12 T. D. Rane, *et al.*, Counting Single Molecules in Sub-Nanolitre Droplets, *Lab Chip*, 2010, **10**, 161–164.
13 M. Srisa Art, A. J. deMello and J. B. Edel, High-Throughput DNA Droplet Assays Using Picoliter Reactor Volumes, *Anal. Chem.*, 2007, **79**, 6682–6689.
14 M. Srisa Art, A. J. deMello and J. B. Edel, High-Efficiency Single-Molecule Detection within Trapped Aqueous Microdroplets, *J. Phys. Chem. B*, 2010, **114**, 15766–15772.
15 R. M. Doornbos, B. G. de Grooth and J. Greve, Experimental and model investigations of bleaching and saturation of fluorescence in flow cytometry, *Cytometry*, 1997, **29**, 204–214.
16 J. Widengren, A. Chmyrov, C. Eggeling, P. A. Lofdahl and C. A. Seidel, Strategies to improve photostabilities in ultrasensitive fluorescence spectroscopy, *J. Phys. Chem. A*, 2007, **111**, 429–440.
17 B. Vazquez, N. Qureshi, L. Oropeza-Ramos and L. F. Olguin, Effect of velocity on microdroplet fluorescence quantified by laser-induced fluorescence, *Lab Chip*, 2014, **14**, 3550–3555.

Published on 02 October 2017. Downloaded by ETH-Zurich on 12/13/2018 3:44:42 PM.

18 M. P. Cecchini, *et al.*, Ultrafast Surface Enhanced Resonance Raman Scattering Detection in Droplet-Based Microfluidic Systems, *Anal. Chem.*, 2011, **83**, 3076–3081.
19 Z. Y. Han, Y. Y. Chang, S. W. N. Au and B. Zheng, Measuring rapid kinetics by a potentiometric method in droplet-based microfluidic devices, *Chem. Commun.*, 2012, **48**, 1601–1603, DOI: 10.1039/c1cc12383a.
20 N. J. Petersen, K. B. Mogensen and J. P. Kutter, Performance of an in-plane detection cell with integrated waveguides for UV/Vis absorbance measurements on microfluidic separation devices, *Electrophoresis*, 2002, **23**, 3528–3536.
21 A. Gaiduk, M. Yorulmaz, P. V. Ruijgrok and M. Orrit, Room-Temperature Detection of a Single Molecule's Absorption by Photothermal Contrast, *Science*, 2010, **330**, 353–356.
22 K. S. Deal and C. J. Easley, Self-Regulated, Droplet-Based Sample Chopper for Microfluidic Absorbance Detection, *Anal. Chem.*, 2012, **84**, 1510–1516.
23 Z. Liang, *et al.*, Microfabrication of a Planar Absorbance and Fluorescence Cell for Integrated Capillary Electrophoresis Devices, *Anal. Chem.*, 1996, **68**, 1040–1046.
24 S. Löbbecke, W. Ferstl, S. Panić and T. Türcke, Concepts for Modularization and Automation of Microreaction Technology, *Chem. Eng. Technol.*, 2005, **28**, 484–493.
25 K. B. Mogensen, N. J. Petersen, J. Hübner and J. P. Kutter, Monolithic Integration of Optical WWaveguide for Absorbance Detection in Microfabricated Electrophoresis Devices, *Electrophoresis*, 2001, **22**, 3930–3938.
26 P. D. Ohlsson, O. Ordeig, K. B. Mogensen and J. P. Kutter, Electrophoresis Microchip with Integrated Waveguide for Simultaneous Native UV Fluorescence and Absorbance Detection, *Electrophoresis*, 2009, **30**, 4172–4178.
27 D. James, *et al.*, High-Sensitivity Online Detection for Microfluidics via Cavity Ringdown Spectroscopy, *RSC Adv.*, 2012, **2**, 5376–5384.
28 A. Llobera, S. Demming, R. Wilke and S. Büttgenbach, Multiple Internal Reflection Poly(dimethylsiloxane) Systems for Optical Sensing, *Lab Chip*, 2007, **7**, 1560–1566.
29 K. W. Ro, K. Lim, B. C. Shim and J. H. Hahn, Integrated Light Collimating System for Extended Optical-Path-Length Absorbance Detection in Microchip-Based Capillary Electrophoresis, *Anal. Chem.*, 2005, **77**, 5160–5166.
30 C. M. Rushworth, G. Jones, M. Fischlechner, E. Walton and H. Morgan, On-Chip Cavity-Enhanced Absorption Spectroscopy Using a White Light-Emitting Diode and Polymer Mirrors, *Lab Chip*, 2015, **15**, 711–717.
31 K. W. Ro, K. Lim, B. C. Shim and J. H. Hahn, Integrated light collimating system for extended optical-path-length absorbance detection in microchip-based capillary electrophoresis, *Anal. Chem.*, 2005, **77**, 5160–5166.
32 R. Maceiczyk, H. Shimizu, D. Müller, T. Kitamori and A. deMello, A Photothermal Spectrometer for Fast and Background-Free Detection of Individual Nanoparticles in Flow, *Anal. Chem.*, 2017, **89**, 1994–1999.
33 C. L. Cassano, K. Mawatari, T. Kitamori and Z. H. Fan, Thermal Lens Microscopy as a Detector in Microdevices, *Electrophoresis*, 2014, **35**, 2279–2291.
34 T. H. H. Le, K. Mawatari, H. Shimizu and T. Kitamori, Detection of Zeptomole Quantities of Nonfluorescent Molecules in a 10^1 nm Nanochannel by Thermal Lens Microscopy, *Analyst*, 2014, **139**, 2721–2725.
35 H. Shimizu, K. Mawatari and T. Kitamori, Sensitive Determination of Concentration of Nonfluorescent Species in an Extended-Nano Channel by Differential Interference Contrast Thermal Lens Microscope, *Anal. Chem.*, 2010, **82**, 7479–7484.
36 A. R. Salmon, *et al.*, Monitoring Early-Stage Nanoparticle Assembly in Microdroplets by Optical Spectroscopy and SERS, *Small*, 2016, **12**, 1788–1796.
37 L. Mazutis, *et al.*, Single-cell analysis and sorting using droplet-based microfluidics, *Nat. Protoc.*, 2013, **8**, 870–891.
38 S. L. Sjostrom, H. N. Joensson and H. A. Svahn, Multiplex analysis of enzyme kinetics and inhibition by droplet microfluidics using picoinjectors, *Lab Chip*, 2013, **13**, 1754–1761.
39 E. Brouzes, *et al.*, Droplet microfluidic technology for single-cell high-throughput screening, *Proc. Natl. Acad. Sci. U. S. A.*, 2009, **106**, 14195–14200.
40 J. U. Shim, *et al.*, Ultrarapid generation of femtoliter microfluidic droplets for single-molecule-counting immunoassays, *ACS Nano*, 2013, **7**, 5955–5964, DOI: 10.1021/nn401661d.
41 C. Sicard, *et al.*, A rapid and sensitive fluorimetric beta-galactosidase assay for coliform detection using chlorophenol red-beta-D-galactopyranoside, *Anal. Bioanal. Chem.*, 2014, **406**, 5395–5403.
42 E. Vanderperren, W. Demare, R. Blust, K. Cooreman and B. Peter, Oestrogenic activity of CPRG (chlorophenol red-β-D-galactopyranoside), a β-galactosidase substrate commonly used in recombinant yeast oestrogenic assays, *Biomarkers*, 2001, **6**, 375–380.
43 K. E. Langley, M. R. Villarejo, A. V. Fowler, P. J. Zamenhof and I. Zabin, Molecular basis of beta-galactosidase alpha-complementation, *Proc. Natl. Acad. Sci. U. S. A.*, 1975, **72**, 1254–1257.
44 A. Huebner, *et al.*, Quantitative detection of protein expression in single cells using droplet microfluidics, *Chem. Commun.*, 2007, 1218–1220.
45 S. Cho, *et al.*, Droplet-Based Microfluidic Platform for High-Throughput, Multi-Parameter Screening of Photosensitizer Activity, *Anal. Chem.*, 2013, **85**, 8866–8872.
46 F. Gielen, *et al.*, Ultrahigh-throughput-directed enzyme evolution by absorbance-activated droplet sorting (AADS), *Proc. Natl. Acad. Sci. U. S. A.*, 2016, **113**, E7383–E7389.
47 L. Frenz, K. Blank, E. Brouzes and A. D. Griffiths, Reliable microfluidic on-chip incubation of droplets in delay-lines, *Lab Chip*, 2009, **9**, 1344–1348.
48 M. Ishiyama, M. Shiga, K. Sasamoto, M. Mizoguchi and P.-G. He, A New Sulfonated Tetrazolium Salt That Produces a Highly Water-Soluble Formazan Dye, *Chem. Pharm. Bull.*, 1993, **41**, 1118–1122.

 This journal is © The Royal Society of Chemistry 2017

49 C. Furusawa, T. Suzuki, A. Kashiwagi, T. Yomo and K. Kaneko, Ubiquity of Log-Normal Distribtions in Intra-Cellular Reaction Dynamics, *Biophysics*, 2005, **1**, 25–31.
50 B. Kintses, *et al.*, Picoliter cell lysate assays in microfluidic droplet compartments for directed enzyme evolution, *Chem. Biol.*, 2012, **19**, 1001–1009.
51 J. C. Baret, *et al.*, Fluorescence-activated droplet sorting (FADS): efficient microfluidic cell sorting based on enzymatic activity, *Lab Chip*, 2009, **9**, 1850–1858.
52 D. C. Duffy, J. C. McDonald, O. J. A. Schueller and G. M. Whitesides, Rapid prototyping of microfluidic systems in poly(dimethylsiloxane), *Anal. Chem.*, 1998, **70**, 4974–4984, DOI: 10.1021/ac980656z.

Published on 02 October 2017. Downloaded by ETH-Zurich on 12/13/2018 3:44:42 PM.